Research Square

Preprints are preliminary reports that have not undergone peer review.
They should not be considered conclusive, used to inform clinical practice,
or referenced by the media as validated information.

Room-Temperature Resistive CO_2 Sensing with Ultrafast Recovery via NP-PSi/CuO/rGO Trilayer Heterojunction

Jia-Chuan Lin
National Taipei University
Jun-Hao Chen
National Taipei University
Chien-Hong Wu
wuchienhung@mx.nthu.edu.tw

National Tsing Hua University
Hsu-Nan Yen
National Taipei University
Kalpana Settu
Indian Institute of Information Technology Design and Manufacturing, Kurnool

Research Article

Keywords: NP-type porous silicon NP-PSi, CO_2 gas sensor, Sol–gel method, Reduced Graphene Oxide (rGO), CuO

Posted Date: August 14th, 2026

DOI: https://doi.org/10.21203/rs.3.rs-10348841/v1

License: This work is licensed under a Creative Commons Attribution 4.0 International License.
Read Full License

Additional Declarations: No competing interests reported.

Abstract

In this work, a trilayer resistive CO_2 gas sensor was developed by combining an NP-type porous silicon (NP-PSi) substrate with a sol-gel-derived copper oxide (CuO) nanofilm and a drop-cast reduced graphene oxide (rGO) overlayer, and its sensing performance was systematically evaluated at room temperature under an applied voltage of 2 V. Scanning electron microscopy confirmed that CuO uniformly infiltrated the pore walls of the porous silicon substrate and that the rGO sheets formed intimate interfacial contact across the composite surface. Compared to the bare NP-PSi reference (recovery time: 47–82 s), incorporation of CuO shortened the recovery time to 5–30 s through charge transfer facilitated by the p-CuO/n-PSi heterojunction; subsequent addition of rGO further reduced recovery time to 3–7 s and the baseline resistance to 420–560 kΩ, attributed to the high-speed electron transport network provided by the rGO overlayer. The NP-PSi/CuO/rGO composite sensor achieved a sensing response of approximately 26.5% at 5.66 vol% CO_2. Compared with room-temperature CO_2 sensors reported in the literature under equivalent measurement definitions, the present work demonstrates orders-of-magnitude improvement in recovery kinetics, confirming the viability of this trilayer architecture for low-power resistive CO_2 gas sensing applications.

Keywords: NP-type porous silicon NP-PSi, CO_2 gas sensor, Sol–gel method, Reduced Graphene Oxide (rGO), CuO

INTRODUCTION

In recent decades, accelerating global industrialization and urbanization have led to a dramatic rise in anthropogenic CO_2 emissions. As the most significant greenhouse gas, CO_2 traps infrared radiation in the atmosphere, driving global warming and climate change. These concerns have generated strong demand for sensors capable of real-time, sensitive CO_2 detection across applications including agricultural management, industrial process control. Among available sensing technologies, resistive metal oxide semiconductor (MOX)-based sensors have attracted the greatest research interest owing to their simple device architecture, low manufacturing cost, direct electrical signal readout, and inherent compatibility with standard semiconductor fabrication processes. Silicon is the foundational material of the modern semiconductor industry, supporting applications from CMOS logic circuits and MEMS to gas sensors. Of particular relevance is porous silicon (PS), which possesses a three-dimensional network of nanoscale pores that dramatically enlarges the specific surface area, providing abundant active adsorption sites, serving as an effective deposition substrate for metal oxide nanoparticles, and remaining fully compatible with very large scale integration (VLSI) processes—making it an ideal platform for high-performance gas sensing[10, 11, 13]. Within the broad landscape of MOX sensing materials, copper oxide (CuO) has attracted considerable attention due to its intrinsic p-type semiconductor behavior, narrow band gap of approximately 1.2–1.9 eV, and its ability to form p-n heterojunctions when combined with n-type metal oxides, which facilitates charge carrier transfer, lowers the activation energy for sensing reactions, and significantly enhances sensitivity. [9, 14, 15]. To further enhance sensor performance, this work incorporates reduced graphene oxide (rGO) as an auxiliary functional material. Derived from graphene oxide through chemical or thermal reduction, rGO retains the outstanding electrical conductivity of pristine graphene while its residual oxygen-containing functional

groups provide chemically active sites for gas molecule adsorption[17]. The large specific surface area and superior electron transport properties of rGO accelerate interfacial electron transfer following CO_2 adsorption reactions at the metal oxide surface, amplify the resistance-change signal, and enable sensing at lower operating temperatures. Motivated by the foregoing considerations, this work aims to develop a resistive CO_2 gas sensor capable of room-temperature operation under a low applied bias of 2 V, by combining porous silicon substrates with CuO nanoparticles and rGO composite sensing layers synthesized via the sol-gel method. By leveraging the large specific surface area of porous silicon, the p-type semiconductor characteristics and heterojunction-forming capability of CuO, and the superior electron transport properties of rGO, this work seeks to achieve a sensing platform with fast recovery kinetics and concentration-distinguishable CO_2 response under low-power, room-temperature conditions, thereby providing a practically viable sensing solution for industrial applications.

Experiment

Fabrication of porous silicon

All silicon substrates used in this study were single-crystal wafers with a (100) crystallographic orientation, single-side polished, and diced into 3×3 cm² square pieces prior to processing. The NP-type silicon substrates were fabricated on 4-inch (100)-oriented wafers comprising a phosphorus-doped n-type epitaxial top layer grown on a boron-doped p-type base substrate, with the n-type epitaxial layer thickness of 40 ± 5% μm and the p-type substrate thickness of 525 ± 25 μm. To ensure surface cleanliness and to effectively remove organic contaminants and native oxide layers, all substrates were sequentially ultrasonicated in acetone, ethanol, and deionized (DI) water for 5 minutes each prior to anodization. The electrolyte solution was composed of HF, C_2H_5OH, and H_2O_2 in a volumetric ratio of 6:24:0.03 c.c., where hydrofluoric acid was sourced as a 49 wt% aqueous solution and hydrogen peroxide was prepared by diluting a commercial 30 wt% aqueous solution to 6 wt%, ensuring reproducibility of the etching conditions. Electrochemical anodization was carried out in a vertical polytetrafluoroethylene (PTFE) cell system[10, 11].

Synthesis and Characterization of CuO Film

All chemical reagents used in this study were of analytical grade and were employed without further purification. To prepare the CuO precursor solution, 0.05 g of copper(II) acetate monohydrate ($Cu(CO_2CH_3)_2·H_2O$, 99% EP) was dissolved in 5 mL of 99.5% ethanol (C_2H_5OH) under continuous magnetic stirring at 60°C until complete dissolution of the copper ions was confirmed. Monoethanolamine (C_2H_7NO, MEA) aqueous solution was subsequently added dropwise to the above solution as a stabilizing agent, and the mixture was maintained under stirring at 60°C for 1 hour, yielding a homogeneous dark blue transparent gel. The resulting gel was allowed to age slowly at room temperature for 24 hours to facilitate complete network formation[9, 14, 15].

Prior to film deposition, the prepared NP-PSi substrates were pre-wetted with ethanol to promote uniform spreading of the precursor solution. The aged precursor solution was then drop-cast onto the

substrate surface and spin-coated sequentially at 1500 rpm for 15 seconds followed by 3000 rpm for 30 seconds, after which the coated substrate was soft-baked at 120°C for 5 minutes to remove residual solvent. This spin-coating and soft-baking procedure was repeated three times in total to achieve a film of adequate and uniform thickness. The samples were subsequently subjected to stepwise thermal annealing in a high-temperature furnace with a temperature increment of 100°C per step, culminating in calcination at 500°C for 1 hour to fully decompose the precursor and promote the formation of crystalline CuO.

Deposition and Characterization of rGO Film

A dispersion of reduced graphene oxide (rGO, carbon content > 82 wt%, ACS Material, LLC) was prepared by dispersing 2 mg of rGO powder in 2 mL of 99.5% ethanol to yield a suspension with a mass ratio of 1:1000. The suspension was subjected to ultrasonic tip sonication using a probe sonicator (GC-150SPro, NBGC Tech) operated at 30% amplitude for 30 minutes to ensure thorough exfoliation and uniform dispersion of the rGO sheets. The resulting dispersion was drop-cast onto the surface of the prepared NP-PSi/CuO samples and subsequently dried in a vacuum oven at 70°C for 15 minutes to remove residual solvent and promote adhesion of the rGO film to the underlying substrate[17].

Characterizations

The surface morphology and cross-sectional microstructure of the NP-PSi, NP-PSi/CuO, and NP-PSi/CuO/rGO samples were examined using a scanning electron microscope (SEM, Hitachi S-3500H). The electrical characteristics of the fabricated devices, including current–voltage (I–V) curves and real-time current response under CO2 exposure (I–t) curves, were systematically recorded at room temperature using a high-precision source measure unit (Keysight B2902A)

Methodology for sensing measurements.

For electrical characterization, interdigitated electrodes were screen-printed onto the surface of each composite sample using silver paste and subsequently cured at 120°C for 30 minutes to remove residual solvent and ensure reliable adhesion between the electrodes and the substrate. The real-time current response under gas exposure (I–t curves) of all samples was systematically recorded at room temperature using a high-precision source measure unit (Keysight B2902A).

The sensing measurement procedure was conducted as follows. Prior to CO_2 introduction, a stable baseline resistance at one atmosphere air (Rair) was established. Once the baseline was stabilized, CO_2 was introduced into the measurement chamber by Mass Flow Controller sequentially at flow rates of 100, 200, 300, 400, and 500 SCCM. Under each flow rate condition, gas exposure was maintained for 100 seconds, after which the gas inlet was closed and the chamber was allowed to recover to ambient atmospheric conditions, completing a single measurement cycle. This procedure was subsequently repeated for three additional cycles to evaluate the repeatability and stability of the sensing response. "For a closed cylindrical chamber with dimensions of Ø250*300mm and a calculated volume of 14.726 L,

the introduction of CO2 gas at the aforementioned flow rates for 100s yields calculated volume concentrations of 1.133%, 2.266%, 3.399%, 4.533%, and 5.566%, respectively."

The response time is defined as the time required for the resistance to reach 90% of the maximum resistance change after gas introduction. The recovery time is defined as the time required for the resistance to return to within 10% of the maximum resistance change after the gas flow is terminated. In this work, the sensing response (S) of the composite structures is defined as:

$$S = \frac{R_{gas} - R_{air}}{R_{air}} \times 100\%$$

where R_{air} is the steady-state resistance measured in ambient air and R_{gas} is the resistance measured upon exposure to CO_2 at each respective flow rate (100, 200, 300, 400, and 500 SCCM). This definition is adopted to quantify the relative change in sensing layer resistance in response to varying CO_2 concentrations, and serves as the primary metric for evaluating and comparing the sensing characteristics of each composite structure investigated in this work.

Results & Discussion

Figure 1(a) and (b) present the surface morphology and cross-sectional structure of the NP-PSi substrate following electrochemical anodization. The surface SEM image reveals a high-density array of uniformly distributed macropores with an average pore diameter of approximately 2 μm and a high overall porosity. The cross-sectional image clearly demonstrates that the pores extend vertically into the silicon substrate to a depth of approximately 10–20 μm, forming a well-defined high-aspect-ratio columnar pore architecture. This three-dimensional interconnected pore network endows the NP-PSi substrate with an exceptionally large effective specific surface area, providing abundant active sites for gas molecule adsorption even prior to the application of any functional modification layer, thereby establishing an ideal structural foundation for subsequent composite material deposition[10,11,13].

Figure 1 (c) and (d) show the surface morphology and cross-sectional images of the NP-PSi/CuO composite structure. Compared to the pristine NP-PSi substrate, the surface of the CuO-deposited sample exhibits a notably denser and more uniform coverage, indicating that the CuO film prepared via the sol-gel process effectively conformally coats the pore walls of the porous silicon substrate. The cross-sectional image further confirms that the CuO precursor solution successfully infiltrated the interior of the pores during the spin-coating and subsequent calcination process, forming a continuous CuO film along the pore walls throughout the full depth of the porous layer. This conformal coating of CuO within the pore structure substantially increases the effective sensing area of the composite relative to a planar CuO film, and simultaneously enhances gas adsorption efficiency by increasing the density of active sites available for CO_2 molecule interaction and by exploiting the pore geometry to concentrate gas molecules in close proximity to the sensing material[9,15].

Figure 1(e) and (f) display the surface morphology and cross-sectional images of the final NP-PSi/CuO/rGO composite structure. The surface SEM image reveals that the rGO sheets uniformly cover the top surface of the NP-PSi/CuO composite in the form of a thin overlying film, exhibiting the characteristic two-dimensional lamellar morphology of reduced graphene oxide. The cross-sectional image demonstrates intimate interfacial contact between the rGO overlayer and the underlying CuO/porous silicon structure, with each constituent layer clearly distinguishable. The incorporation of rGO not only provides supplementary gas adsorption sites on the composite surface through its residual oxygen-containing functional groups, but its outstanding electron transport properties also effectively accelerate the transfer of electrons released during the reaction between CO_2 molecules and the oxygen species adsorbed on the CuO surface, thereby amplifying the measurable resistance-change signal and enhancing the overall sensing response. Taken together, the morphological analysis confirms that the NP-PSi/CuO/rGO trilayer composite structure successfully integrates the large specific surface area of porous silicon, the p-type semiconductor sensing characteristics of CuO, and the superior electrical conductivity of rGO into a synergistic architecture that provides a robust structural foundation for CO_2 gas sensing[10,11,18].

Prior to discussing the sensing performance of the composite structures, it is necessary to first elucidate the physical sensing mechanism of the unmodified NP-PSi substrate, which serves as the reference baseline for subsequent comparison. The electrical behavior of the NP-PSi device is governed by its distinctive bilayer architecture: the uppermost layer consists of a phosphorus-doped n-type porous silicon film that is directly exposed to the gas environment and constitutes the primary conductive channel for interaction with CO_2 molecules, while the underlying boron-doped p-type silicon substrate forms an NP junction at the interface between the two layers.

Upon introduction of CO_2 into the measurement chamber, the oxidizing CO_2 molecules adsorb onto the surface of the n-type porous silicon layer and withdraw free electrons from the semiconductor surface, causing the surface depletion layer of the n-type silicon to widen significantly. Since the pore wall thickness of the porous silicon structure is on the order of only a few micrometers, the expansion of the depletion layer directly compresses the effective cross-sectional area available for electron transport within the pore walls, resulting in a measurable increase in the overall device resistance. Concurrently, the reduction in free electron concentration at the n-type layer surface causes a downward shift of the Fermi level in the n-type layer, which in turn perturbs the band alignment at the NP junction: the built-in electric field and barrier height at the junction are modified accordingly, increasing the difficulty for charge carriers to traverse the junction under a given applied bias. This synergistic amplification effect of the NP junction makes the resistance response of NP-PSi to CO_2 more pronounced than would be observed in a simple n-type structure alone[13].

Figure 6 (a) presents the resistance–time (R–t) response curves of the NP-PSi sample recorded over three consecutive measurement cycles at CO_2 flow rates of 100, 200, 300, 400, and 500 SCCM, respectively. Under all flow rate conditions, the baseline resistance values fall within a relatively high range of approximately 1.6 to 2.0 MΩ. This elevated baseline resistance is attributable to the geometric

scattering effect introduced by the extensive pore network of the porous silicon structure, which drastically reduces the effective conductive cross-section along the current path, compounded by the barrier effect of the NP junction. With regard to the trend of the response curves, the resistance increases upon CO_2 introduction and gradually recovers after the gas flow is terminated, consistent with the physical mechanism of surface depletion layer expansion and subsequent desorption of CO_2 molecules from the porous silicon surface. The recovery process is notably slow, reflecting the limited desorption rate of CO_2 molecules from the unmodified porous silicon surface. Furthermore, as the CO_2 flow rate is increased from 100 to 500 SCCM, the magnitude of the resistance change exhibits a progressive increase, consistent with the expected behavior arising from the greater number of adsorbed gas molecules at higher concentrations. It is also noted that the response curve at 500 SCCM exhibits markedly increased noise, which is tentatively attributed to measurement perturbations induced by the mechanical impact of the high-velocity gas flow on the device.

As summarized in Figure 7 (a) , the response time of NP-PSi—defined as the time required for the resistance to reach 90% of its maximum change—falls in the range of 83 to 95 seconds, while the recovery time—defined as the time required for the resistance to return to within 10% of the maximum resistance change—ranges from 47 to 82 seconds. These values indicate that the adsorption and desorption kinetics of NP-PSi are relatively slow, which is attributed to the absence of catalytically active surface sites on the unmodified porous silicon surface that could facilitate the chemisorption and desorption of CO_2 molecules. On this basis, the NP-PSi sample is designated as the reference control in this study, and its sensing performance will be systematically compared with that of the CuO- and rGO-functionalized composite structures in the subsequent sections, in order to quantitatively evaluate the individual contributions of each functional layer to the overall sensing response speed and sensitivity.

To evaluate the improvement in sensing performance afforded by the CuO functional layer, a systematic gas sensing characterization of the NP-PSi/CuO composite structure was conducted, using the NP-PSi sample discussed in the preceding section as the reference baseline.

Figure 2(a) presents the real-time sensitivity–time curves of the NP-PSi/CuO sample recorded under a constant applied voltage of 2 V during 100-second CO_2 exposure intervals at flow rates ranging from 100 to 500 SCCM. Under all flow rate conditions, the sensitivity increases continuously with gas exposure time, and the sensitivity curves for different flow rates exhibit a clear concentration-dependent stratification, with higher flow rates corresponding to higher sensitivity values, indicating a well-defined flow-rate response relationship for the NP-PSi/CuO composite. Notably, compared to the NP-PSi reference, the measurement noise under high flow rate conditions (400 and 500 SCCM) is substantially reduced, suggesting that the incorporation of the CuO functional layer effectively mitigates the electrical measurement perturbations induced by high-velocity gas impingement, yielding smoother and more stable sensing signals.

Figure 6 (b) presents the resistance–time (R–t) response curves of the NP-PSi/CuO sample over three consecutive measurement cycles at CO_2 flow rates of 100, 200, 300, 400, and 500 SCCM, respectively,

together with detailed analyses of the response and recovery times for each individual cycle on Figure 3 (a) through (e). Compared to the NP-PSi reference, the baseline resistance of the NP-PSi/CuO composite is slightly reduced, falling within the range of approximately 1.1 to 1.5 MΩ. This marginal reduction in baseline resistance is attributed to the introduction of p-CuO nano-islands, which provide additional hole-mediated conduction pathways within the composite system. However, the most significant improvement observed in the NP-PSi/CuO composite relative to the NP-PSi reference lies in the substantially shortened response and recovery times.

The physical mechanism underlying this kinetic improvement is as follows. Following calcination at 500°C, the CuO derived from the 0.05 M copper acetate precursor solution is distributed as sparse nano-islands conformally lining the inner pore walls of the n-type porous silicon, forming numerous localized p-CuO/n-PSi heterojunctions at the CuO/PSi interface. Upon adsorption of CO_2 molecules onto the p-CuO surface, the oxidizing nature of CO_2 withdraws electrons from the CuO surface, causing a relative increase in hole concentration within the p-CuO and further enhancing its p-type character, with a concomitant downward shift of the CuO Fermi level. This Fermi level shift intensifies the built-in electric field at the p-CuO/n-PSi heterojunction interface, compelling the depletion layer within the underlying n-type porous silicon pore walls to widen significantly inward. Since the pore wall skeleton of the porous silicon is inherently thin—on the order of only a few micrometers—the inward expansion of the depletion layer exerts pinch-off effect on the effective conductive cross-section available for electron transport within the n-type layer, causing the overall device resistance to rise sharply. This charge transfer mechanism mediated by the p-CuO/n-PSi heterojunction provides a more sensitive and rapid signal amplification pathway compared to the sole mechanism operative in pristine NP-PSi, where CO_2 must directly withdraw electrons from the n-type silicon surface.

Regarding the morphology of the response curves, the resistance exhibits a smooth and continuously rising profile upon CO_2 introduction, which is consistent with the physical process of dynamic diffusion and progressive adsorption of CO_2 molecules within the deep porous channels extending 10–20 μm into the substrate—gas molecules permeate gradually from the pore opening toward the pore bottom, sequentially occupying available adsorption sites and producing a steady, monotonically increasing resistance response rather than an abrupt step change. From the quantitative response and recovery time data extracted for each flow rate condition, the response time (Rise Time) decreases progressively from 49.98 seconds at 100 SCCM to 40.85 seconds at 200 SCCM, 36.67 seconds at 300 SCCM, 35.06 seconds at 400 SCCM, and 36.53 seconds at 500 SCCM; the recovery time (Fall Time) decreases markedly from 29.11 seconds at 100 SCCM to 24.40 seconds at 200 SCCM, 17.29 seconds at 300 SCCM, 15.67 seconds at 400 SCCM, and 9.23 seconds at 500 SCCM as summarized in Figure 7 (b). In comparison with the NP-PSi reference, which exhibited response times of 83–95 seconds and recovery times of 47–82 seconds, the NP-PSi/CuO composite achieves substantial improvements in both response and recovery kinetics, clearly validating the effectiveness of the CuO functional layer in enhancing sensing dynamics through the p-n heterojunction mechanism[1,5,6].

Nevertheless, the recovery curves of the NP-PSi/CuO composite under certain flow rate conditions—most notably at 300 and 500 SCCM—still exhibit a degree of irregular fluctuation, suggesting that the electron transport efficiency of the composite structure has not yet been fully optimized in the absence of an additional conductive auxiliary layer. Motivated by this observation, the present study further incorporates an rGO functional overlayer onto the NP-PSi/CuO structure to construct the NP-PSi/CuO/rGO trilayer composite, which constitutes the primary experimental group of this work. It is anticipated that the superior electron transport properties and abundant surface adsorption sites of rGO will synergistically complement the heterojunction-based sensing mechanism of CuO, comprehensively enhancing the sensor's sensitivity, response speed, and signal stability. The corresponding sensing results will be presented and discussed in detail in the following section[12,18].

Having established that the NP-PSi/CuO composite structure affords substantially improved sensing performance relative to the bare NP-PSi substrate, this section presents a comprehensive gas sensing characterization of the NP-PSi/CuO/rGO trilayer composite—the primary experimental group of this study—to systematically evaluate the actual contribution of the rGO functional overlayer to the overall sensing performance.

Figure 2(b) presents the real-time sensitivity–time curves of the NP-PSi/CuO/rGO sample recorded under a constant applied voltage of 2 V during 100-second CO_2 exposure intervals at flow rates ranging from 100 to 500 SCCM. Compared to the NP-PSi/CuO reference, the incorporation of the rGO overlayer yields a marked enhancement in sensitivity, most prominently at high flow rate conditions: at 500 SCCM, the sensitivity reaches approximately 26.5%, substantially exceeding the approximately 16.5% achieved by NP-PSi/CuO and the approximately 11% exhibited by NP-PSi under the same conditions. Furthermore, the sensitivity curves exhibit an exceptionally steep initial rise during the first 0–10 seconds of gas exposure, rapidly approaching a near-plateau value within approximately 10–20 seconds, indicating that the NP-PSi/CuO/rGO composite possesses a remarkably fast initial response to CO_2. Particularly noteworthy is the behavior observed immediately following gas termination at t = 100 seconds: the sensitivity curves exhibit a near-vertical, near-instantaneous drop back to zero across all flow rate conditions—a rapid recovery characteristic not observed in either of the preceding two sample groups—clearly demonstrating the decisive contribution of rGO's superior electron transport capability to the recovery kinetics of the sensor.

Figure 6(c) presents the resistance–time (R–t) response curves of the NP-PSi/CuO/rGO sample over three consecutive measurement cycles at CO_2 flow rates of 100, 200, 300, 400, and 500 SCCM, respectively, together with detailed single-cycle analyses of the response and recovery times at each flow rate on Figure 4(a) through (e). The most structurally significant distinction relative to the NP-PSi/CuO reference is the dramatic reduction in baseline resistance: the NP-PSi/CuO/rGO composite exhibits baseline resistance values in the range of approximately 420–560 kΩ, representing a reduction of approximately 2–3-fold compared to the 1.1–1.5 MΩ of NP-PSi/CuO and more than 3-fold compared to the 1.6–2.0 MΩ of NP-PSi. This substantial reduction in baseline resistance directly reflects the formation of a highly efficient two-dimensional electron transport network provided by the rGO film

overlying the composite structure, which introduces a low-resistance parallel conduction pathway that fundamentally improves the overall electrical conductivity of the device and reduces the system's series resistance.

With regard to the quantitative response and recovery kinetics, the response time (Rise Time) values extracted from the single-cycle analyses are 48.72 seconds at 100 SCCM, 37.20 seconds at 200 SCCM, 40.39 seconds at 300 SCCM, 48.50 seconds at 400 SCCM, and 32.64 seconds at 500 SCCM. The recovery time (Fall Time) values are 5.08 seconds at 100 SCCM, 4.05 seconds at 200 SCCM, 6.50 seconds at 300 SCCM, 3.18 seconds at 400 SCCM, and 4.78 seconds at 500 SCCM ss summarized in Figure 7 (c). The improvement in recovery time is particularly striking: compared to the NP-PSi/CuO reference, whose recovery times ranged from 5.28 to 29.11 seconds, all recovery times of the NP-PSi/CuO/rGO composite fall below 10 seconds, with the minimum reaching as low as 3.18 seconds at 400 SCCM. This comprehensive reduction in recovery time across all flow rate conditions unambiguously validates the decisive role of the high-speed electron transport pathways provided by rGO in accelerating the redistribution of charge carriers following CO_2 desorption[12,18]. The three-cycle R–t curves also exhibit good periodicity and consistency, demonstrating the excellent repeatability and operational stability of the composite sensor.

Figure 5. presents a comparative summary of the sensitivity of all three sensor structures—NP-PSi, NP-PSi/CuO, and NP-PSi/CuO/rGO—as a function of CO_2 volume concentration, spanning a range of 1.13% to 5.66% vol% corresponding to flow rates of 100 to 500 SCCM applied for 100 seconds, with all data points sampled at 90% of the maximum sensitivity achieved under each condition. All three structures exhibit a monotonically increasing sensitivity with increasing CO_2 concentration, yet with markedly different magnitudes and trends. NP-PSi displays a nearly flat, low-sensitivity response throughout the entire concentration range, with sensitivity values confined between approximately 10% and 11%, reflecting the inherent limitation imposed by the absence of catalytically active surface sites on the unmodified porous silicon surface. NP-PSi/CuO shows a significant improvement over NP-PSi, with sensitivity increasing linearly from 13% to 16.5% across the 1.13%–5.66% concentration range, corroborating the sensitization afforded by the p-CuO/n-PSi heterojunction mechanism. The NP-PSi/CuO/rGO experimental group exhibits sensitivity values comparable to NP-PSi/CuO at low concentrations (1.13%–3.40%), but displays a sharply accelerating, nonlinear enhancement at higher concentrations (4.53%–5.66%), reaching approximately 26.5% at 5.66% CO_2—far exceeding the 16.5% of NP-PSi/CuO at the same concentration. This nonlinear sensitivity enhancement at high concentrations is attributed to the synergistic co-adsorption effect arising when a large flux of CO_2 molecules simultaneously interacts with both the residual oxygen-containing functional groups on the rGO surface and the adsorbed oxygen species on the CuO surface, an effect that becomes fully operative and mutually amplifying only at sufficiently high gas concentrations.

Taken together, the results presented in this section demonstrate that the NP-PSi/CuO/rGO trilayer composite achieves comprehensive improvements in sensitivity, response speed, and recovery dynamics through multiple synergistic mechanisms: the exceptionally large specific surface area of the

porous silicon substrate, the charge transfer amplification effect of the p-CuO/n-PSi heterojunction, and the high-speed electron transport and supplementary adsorption functionality provided by the rGO overlayer. The findings of this study conclusively establish that the incorporation of rGO constitutes the critical material strategy for elevating the overall performance of the NP-PSi/CuO sensing platform, and provide an important materials design framework for the future development of high-performance, room-temperature-operable resistive CO_2 gas sensors.

CONCLUSIONS

In this work, a trilayer resistive CO_2 gas sensor was developed by combining an NP-type porous silicon (NP-PSi) substrate with a sol-gel-derived copper oxide (CuO) nanofilm and a drop-cast reduced graphene oxide (rGO) overlayer, and its sensing performance was systematically evaluated at room temperature under an applied voltage of 2 V. Scanning electron microscopy confirmed that CuO uniformly infiltrated the pore walls of the porous silicon substrate and that the rGO sheets formed intimate interfacial contact across the composite surface. Compared to the bare NP-PSi reference (recovery time: 47–82 s), incorporation of CuO shortened the recovery time to 5–30 s through charge transfer facilitated by the p-CuO/n-PSi heterojunction; subsequent addition of rGO further reduced recovery time to 3–7 s and the baseline resistance to 420–560 kΩ, attributed to the high-speed electron transport network provided by the rGO overlayer. The NP-PSi/CuO/rGO composite sensor achieved a sensing response of approximately 26.5% at 5.66 vol% CO_2. Compared with room-temperature CO_2 sensors reported in the literature under equivalent measurement definitions, the present work demonstrates orders-of-magnitude improvement in recovery kinetics, confirming the viability of this trilayer architecture for low-power resistive CO_2 gas sensing applications.

Declarations

Source(s) of support in the form of grants/funding: None

Ethical Consideration:

This work was supported in part by the National Science and Technology Council of Taiwan for the financial support under Grant No: NSTC 114-2221-E-305-013-

Conflicts of Interest of each author/ contributor:

The authors declare that they have no known competing financial interests or personal relationships that could have appeared to influence the work reported in this paper. This research was conducted in an environment of academic independence, and the results and conclusions are presented without any commercial or personal bias.

A statement that the manuscript has been read and approved by all the authors:

The manuscript has been read and approved by all the authors.

***Co-Corresponding author:**

Chien-Hung Wu, PhD

Affiliations: Department of Education and Learning Technology, National Tsing Hua

University, Hsinchu, Taiwan

Email: wuchienhung@mx.nthu.edu.tw

Mobile: +886 921229285

ORCID https://orcid.org/0000-0002-3174-7516

Acknowledgement: This work was supported in part by the National Science and Technology Council of Taiwan for the financial support under Grant No: NSTC 114-2221-E-305-013-

DATA AVAILABILITY STATEMENTS

Data are available from the Corresponding Author upon request
at: wuchienhung@mx.nthu.edu.tw

Author Contributions (CRediT):

- J.-C.L.: Conceptualization, Methodology, Writing - Original Draft.
- J.-H.C.: Methodology, Writing - Original Draft, Investigation, Data Curation.
- C.-H.W.: Supervision, Project Administration, Resources, Funding Acquisition, Writing - Review & Editing.
- H.-N.Y.: Formal Analysis, Validation.
- K. Settu .: Technological support

References

1. T. Thomas, Y. Kumar, J.A.R. Ramón}, V. Agarwal, S.S. Guzmán}, R. R, S. Pushpan, S.L. Loredo, K.C. Sanal, Vacuum. **184**, 109983 (2021). https://doi.org/10.1016/j.vacuum.2020.109983
2. T.A. Taha, R. Saad, M. Zayed, M. Shaban, A.M. Ahmed, Appl. Phys. A **129**, 115 (2023). https://doi.org/10.1007/s00339-023-06387-6
3. M. Bahar, M. Gholami, M.E. Azim-Araghi, Mater. Sci. Semiconduct. Process. **26**, 491 (2014). http://doi.org/10.1016/j.mssp.2014.05.035
4. D.M.R. Gonzalez}, Y. Kumar, J.A.R. Ramón}, N.K.R. Bogyreddy, S.F. Olive-Méndez, T.V.K. Karthik, D. Becerra, E. Pérez-Tijerina, V. Agarwal, Sens. Int. **3**, 100165 (2022). https://doi.org/10.1016/j.sintl.2022.100165

5. T.V.K. Karthik, L. Martinez, V. Agarwal, J. Alloys Compd. **731**, 853 (2018). https://doi.org/10.1016/j.jallcom.2017.10.070
6. L. Martínez, J.T. Holguín-Momaca, T.V.K. Karthik, S.F. Olive-Méndez, J. Campos-Alvarez, V. Agarwal, Superlattices Microstruct. **98**, 8 (2016). https://doi.org/10.1016/j.spmi.2016.07.028
7. M. Mishra, M. Kumar, Phys. Scr. **99**, 125929 (2024). https://doi.org/10.1088/1402-4896/ad8526
8. C.K. Nerkar, S.G. Shinde, V.S. Raut, S.A. Shaikh, S.S. Chobe, J. Indian Chem. Soc. **102**, 101751 (2025). https://doi.org/10.1016/j.jics.2025.101751
9. F. Wang, H. Li, Z. Yuan, Y. Sun, F. Chang, H. Deng, L. Xie, H. Li, RSC Adv. **6**, 79343 (2016). https://doi.org/10.1039/c6ra13876d
10. G. Korotcenkov, B.K. Cho, Crit. Rev. Solid State Mater. Sci. **35**, 1 (2010). https://doi.org/10.1080/10408430903245369
11. V.A. Moshnikov, I. Gracheva, A.S. Lenshin, Y.M. Spivak, M.G. Anchkov, V.V. Kuznetsov, J.M. Olchowik, J. Non-cryst. Solids. **358**, 590 (2012). https://doi.org/10.1016/j.jnoncrysol.2011.10.017
12. J.A. Ramos-Ramón, N.K.R. Bogireddy, J.A. Giles Vieyra, T.V.K. Karthik, V. Agarwal, Front. Chem. **8**, 291 (2020). https://doi.org/10.3389/fchem.2020.00291
13. E. Kayahan, Optik. **164**, 271 (2018). https://doi.org/10.1016/j.ijleo.2018.03.024
14. M. Habib, S.S. Hussain, S. Riaz, S. Naseem, Materials Today: Proceedings 2, 5714 (2015). https://doi.org/10.1016/j.matpr.2015.11.116
15. M. Patel, S. Mishra, R. Verma, D. Shikha, Discover Mater. **2**, 1 (2022). https://doi.org/10.1007/s43939-022-00022-6
16. L. Dörner, C. Cancellieri, B. Rheingans, M. Walter, R. Kägi, P. Schmutz, M.V. Kovalenko, L.P.H. Jeurgens, Sci. Rep. **9**, 11758 (2019). https://doi.org/10.1038/s41598-019-48020-8
17. Y. Yang, X. Yang, W. Yang, S. Li, J. Xu, Y. Jiang, RSC Adv. **4**, 42546 (2014). https://doi.org/10.1039/c4ra06560c

Table 1

TABLE 1. The performance of forty samples in the study compared with the references.

Sensing Material	Operating Temp.	Applied Voltage	Sensitivity	Response Time (s)	Recovery Time (s)	CO_2 Conc.	Reference
NP-PSi/CuO /rGO	**RT✓**	**2 V ✓**	**~26.5%**	**32–65 ✓**	**3–7 ✓**	**1.13–5.66 vol%**	**This work**
ZnO nanofilms (@ 12h)	RT	0–10 V	28.7%	~684	~228	40–180 SCCM	Taha et al. (2023) [2]
TiO_2/Porous poly-Si	RT	N/A	2–2.32	95	110	10 vol%	Bahar et al. (2014) [3]
Pt–SnO_2 /p-Si	100°C	N/A	~19	~50	~30	10–100 ppm	Ramos González et al. (2022) [4]
p-Si/α-MoO_3	250°C	N/A	12.08%	8	15	50–150 ppm	Thomas et al. (2020) [1]
5% Al-doped ZnO	~227°C	N/A	~103%	80–90	130–155	50–100 ppm	Mishra et al. (2024) [7]
ZnO/p-Si (sputtered)	300°C	N/A	~9.9	~57	~107	1–15 vol%	Martínez et al. (2016) [6]
CuO–MgO	80°C	+30 VDC	93.15%	8	39	100–1000 ppm	Nerkar et al. (2025) [8]

Figures

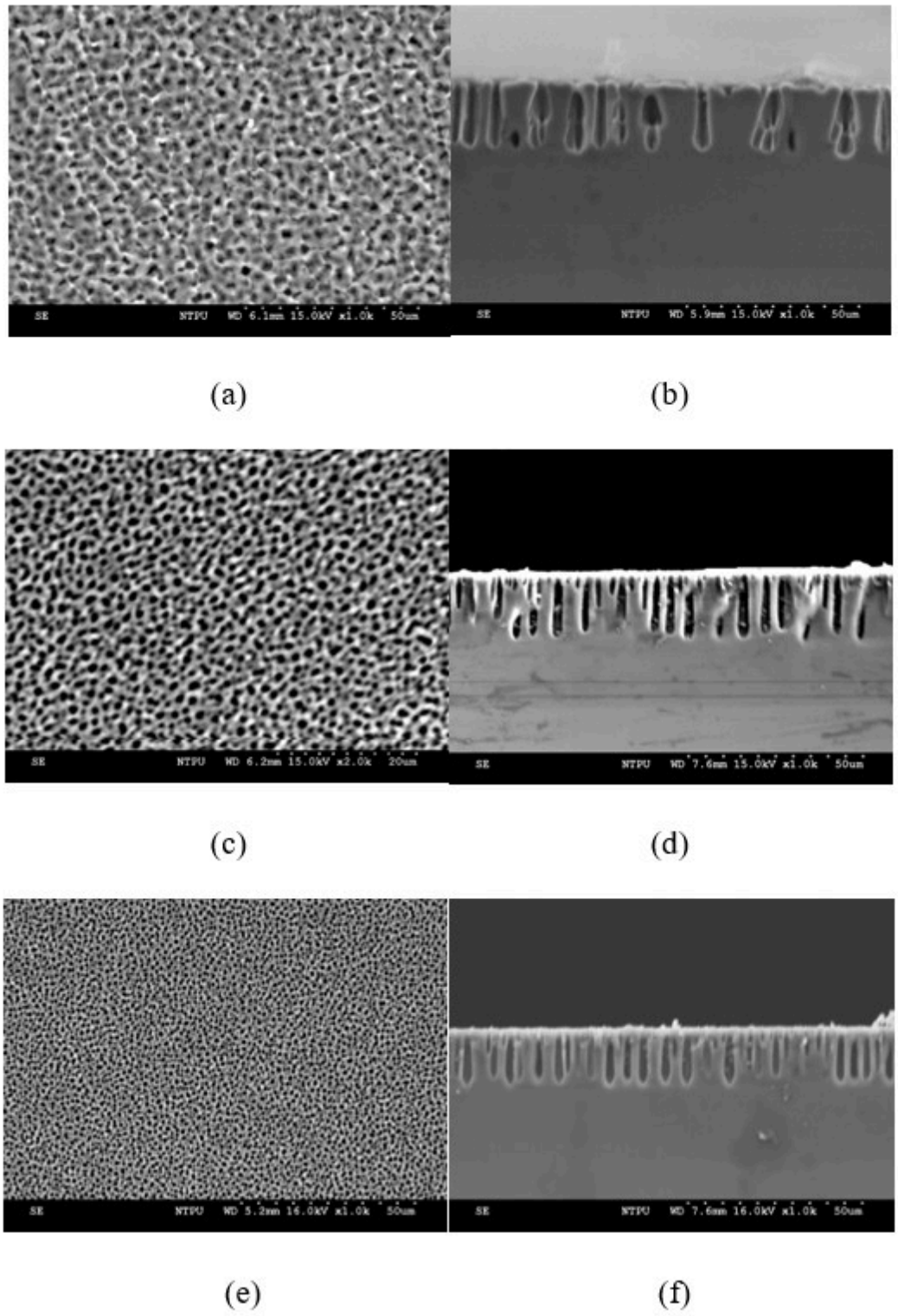


Figure 1

SEM micrographs corresponding to (a) NP-PSi top-view (b)NP-PSi cross-sectional view (c) NP-PSi/CuO top-view (d) NP-PSi/CuO cross-sectional view (e) NP-PSi/CuO/rGO top-view (f) NP-PSi/CuO/rGO cross-sectional view

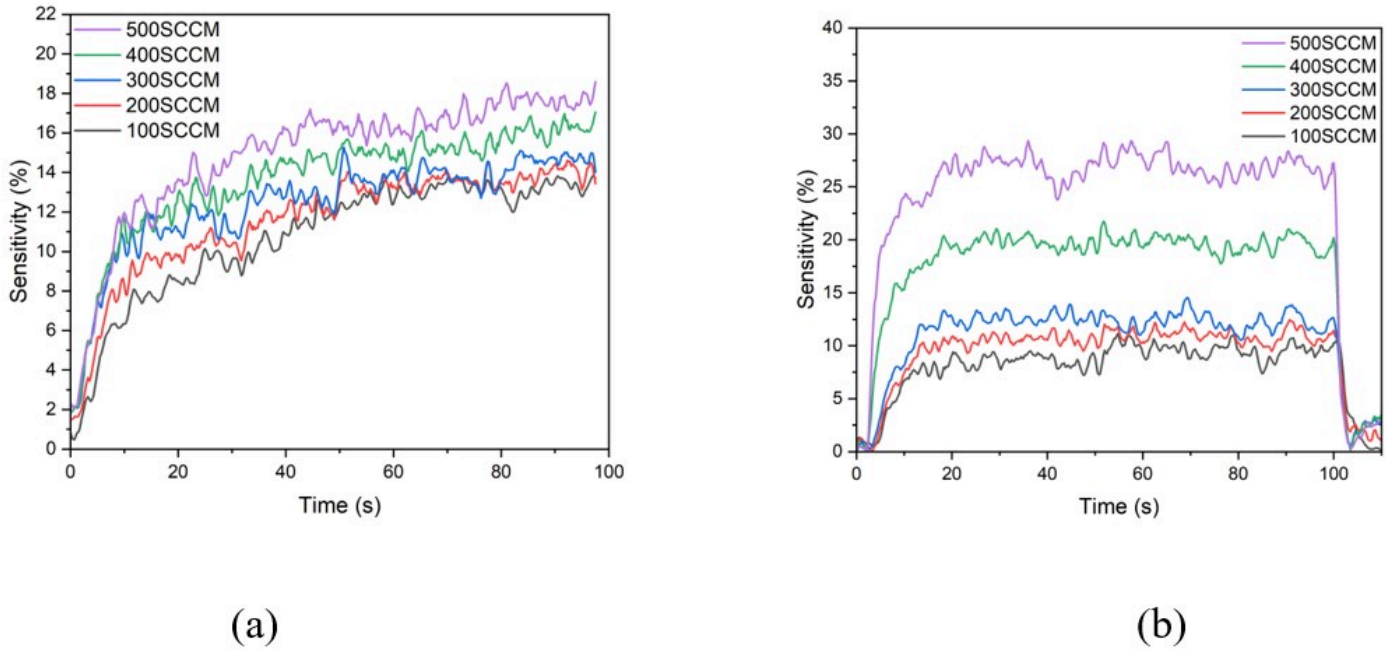


Figure 2

Real-Time sensitivity–time curves of(a)NP-PSi/CuO and(b)NP-PSi/CuO/rGO

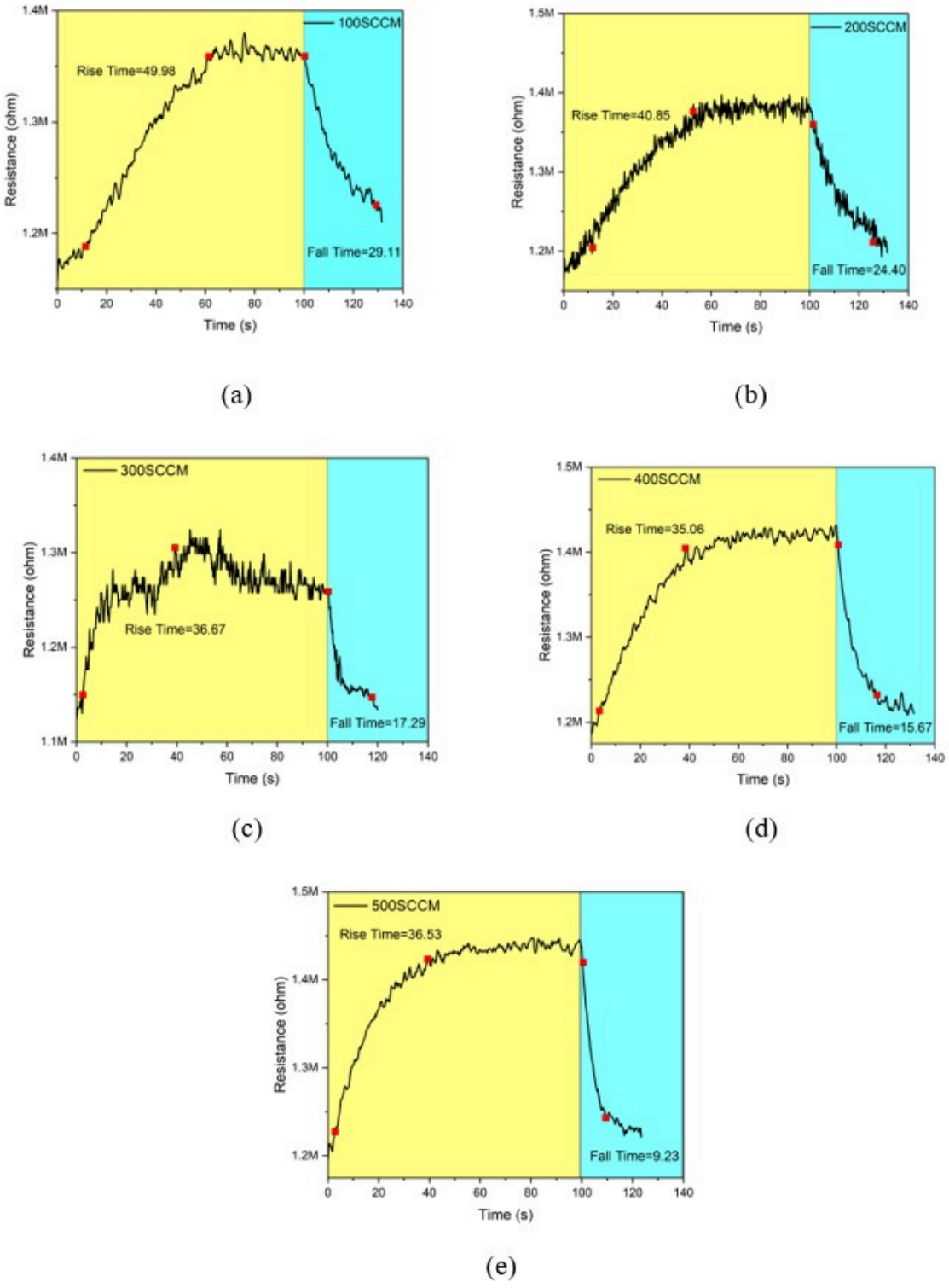


Figure 3

Detailed analyses of the response and recovery times for each individual cycle NP-PSi/CuO sample at CO_2 flow rates of (a)100, (b)200, (c)300, (d) 400, and (e)500 SCCM.

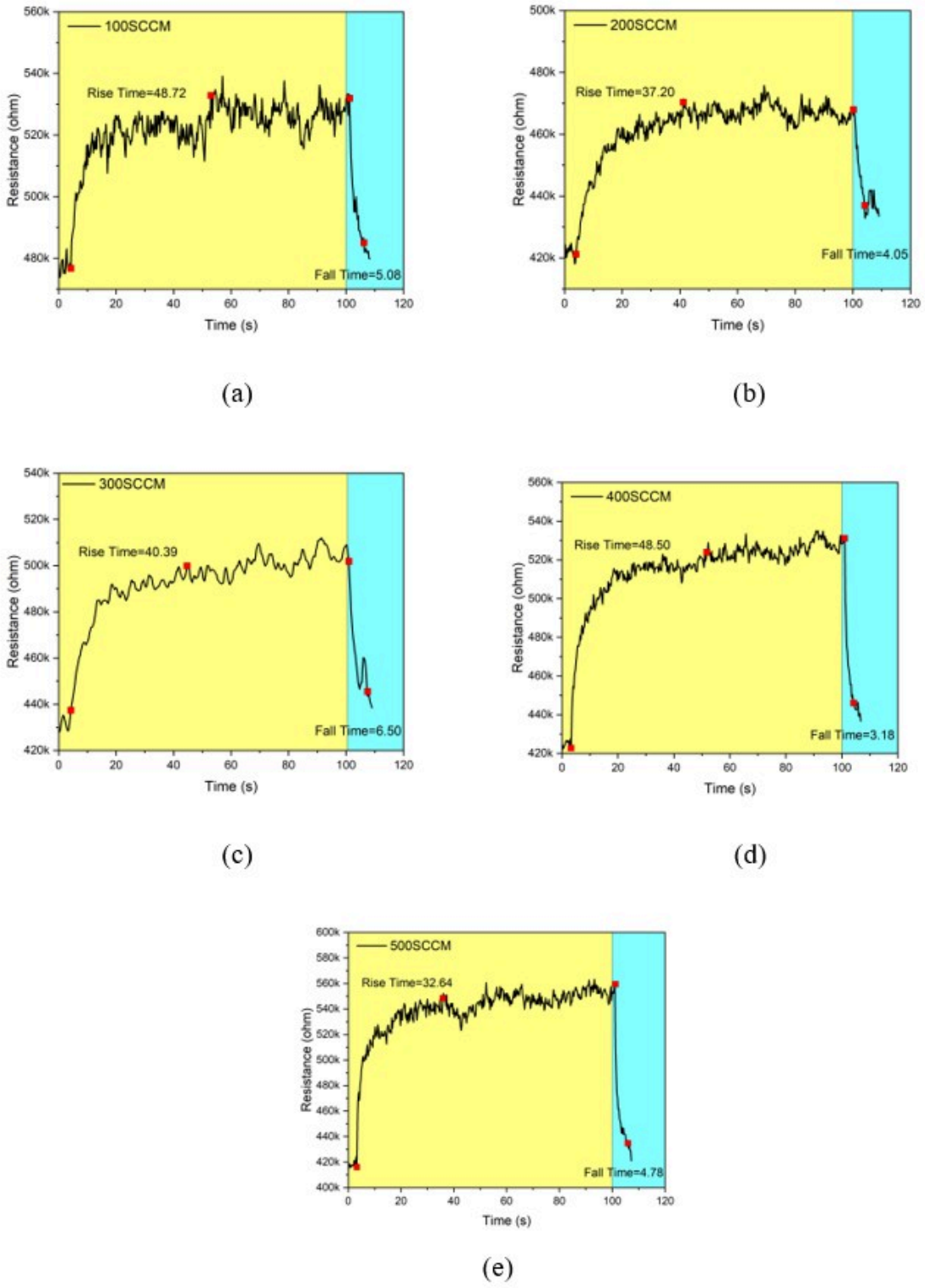


Figure 4

Detailed analyses of the response and recovery times for each individual cycle NP-PSi/CuO/rGO sample at CO_2 flow rates of (a)100, (b)200, (c)300, (d) 400, and (e)500 SCCM.

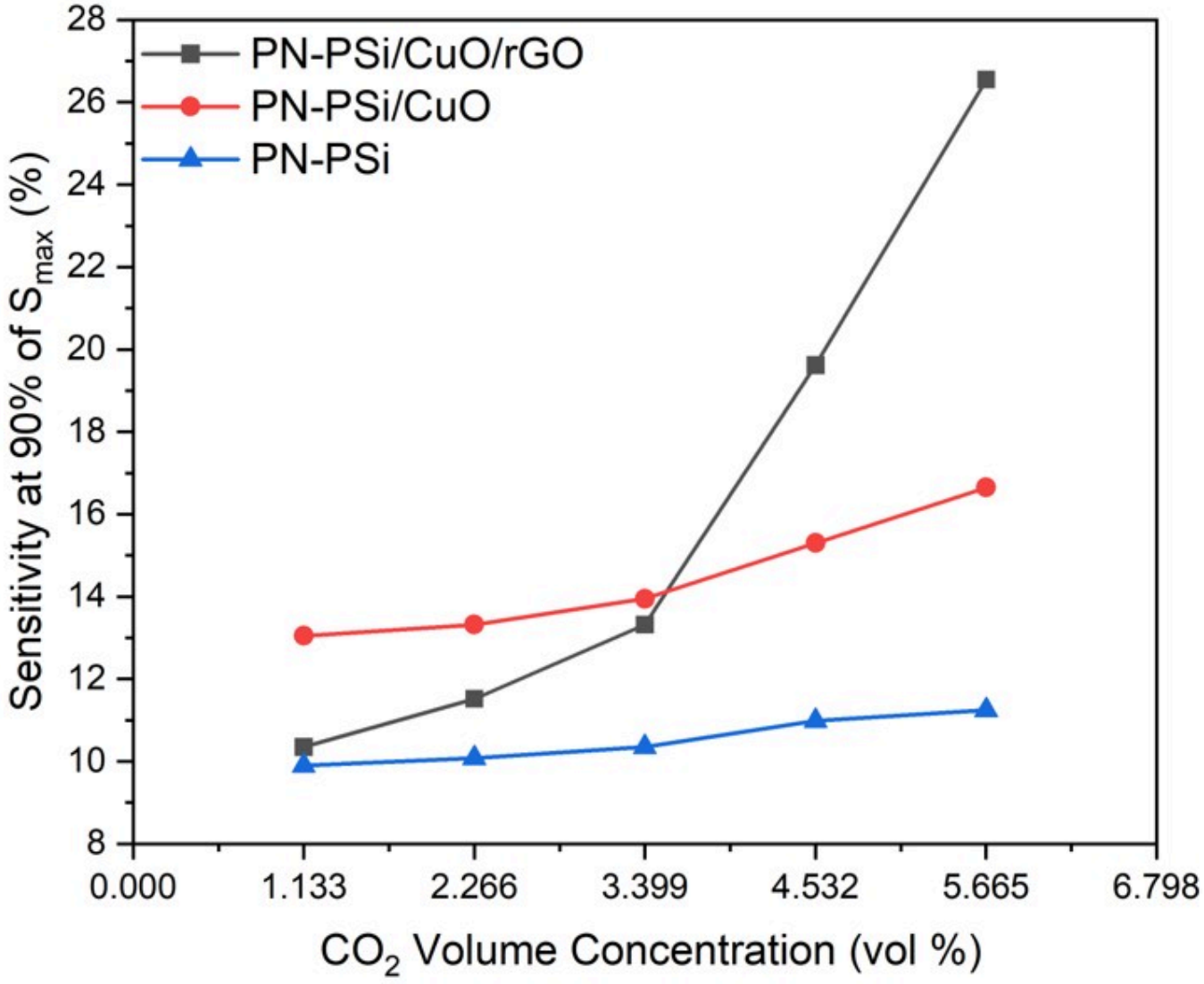


Figure 5

Summary of the sensitivity of all three sensor structures

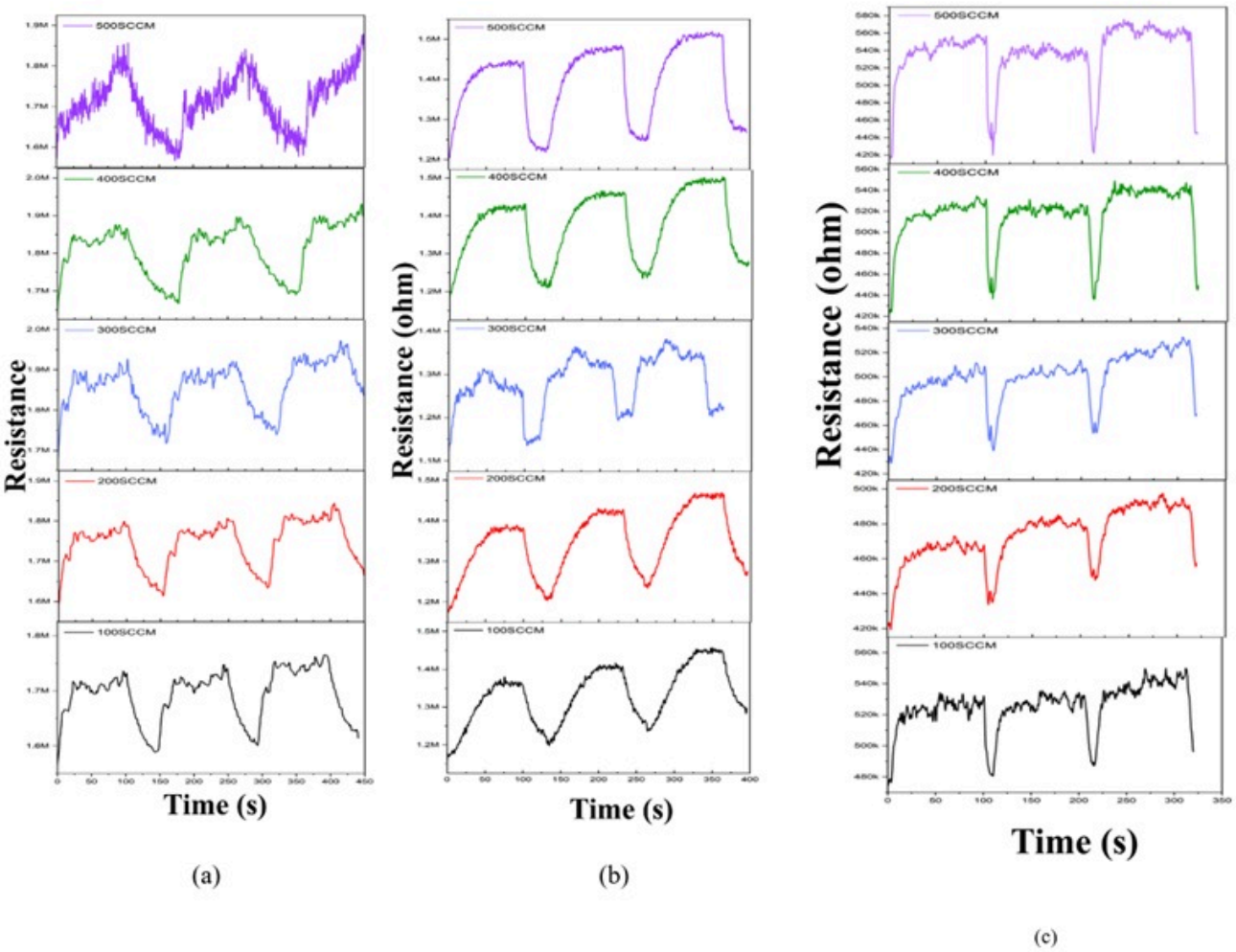
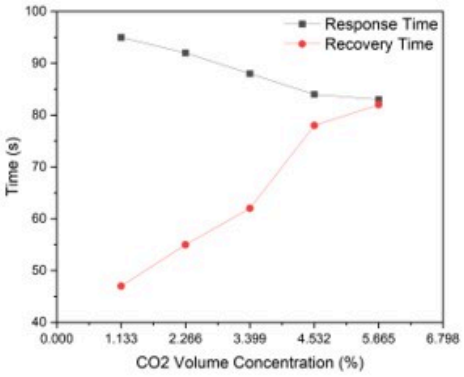
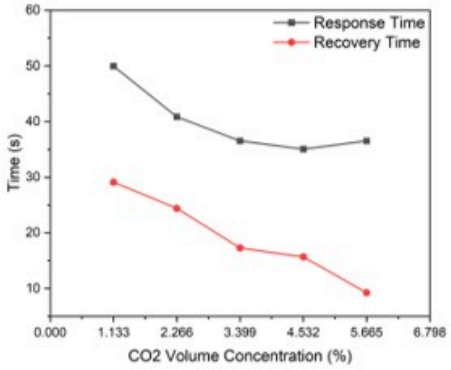


Figure 6

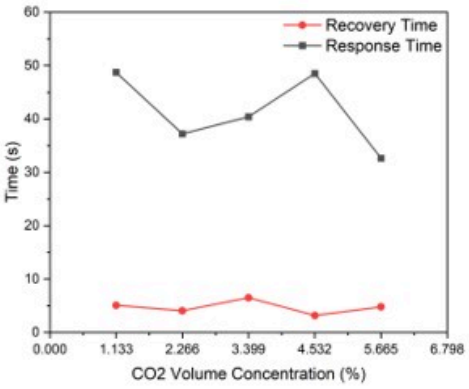
3 Cycle of CO2 Resistance response by (a) NP-PSi, (b) NP-PSi/CuO and(c) NP-PSi/CuO/rGO.



(a)



(b)



(c)

Figure 7

The response time & recovery Time of (a) NP-PSi, (b) NP-PSi/CuO and(c) NP-PSi/CuO/rGO

Supplementary Files

This is a list of supplementary files associated with this preprint. Click to download.

- AuthorContributions.docx